Measurements of length effects on the dynamics of rigid fibers in a turbulent channel flow

Subhani Shaik, Sofia Kuperman ⬤, Vladislav Rinsky, and René van Hout ⬤*
Faculty of Mechanical Engineering, Technion - Israel Institute of Technology, Haifa City, Haifa, Israel

We present experiments on rigid, nylon fiber translation, orientation, and rotation dynamics (one-way coupled) in a fully developed turbulent channel flow (Friction Reynolds number, $\mathrm{Re}_\tau = 435$). The experiments were performed using two-orthogonal view, digital inline Fraunhofer holographic cinematography that allowed us to track individual fibers and determine their three-dimensional (3D) position and orientation along tracks. The research focused on fiber length effects, and two fiber types having similar Stokes numbers but different mean lengths, $\overline{L}^+$ (=27.7 and 50.8), were investigated. Time-resolved data were acquired in the buffer layer, the log layer, and the wake region of the turbulent boundary layer. In the buffer layer irrespective of length, fibers moved faster than the fluid, presumably as a result of fiber accumulation in high-speed streaks. Beyond the buffer layer fibers lagged the fluid, more so for the longest fibers due to increased drag. Probability density functions of instantaneous components of fiber velocities showed that the longest fibers exhibit increased probabilities of "extreme" transverse and wall-normal velocities, mostly in the log layer and the wake region. This is attributed to their interaction with larger, more energetic turbulence structures. Significant fiber-wall interactions were absent, even for the longest fibers due to fiber preferential alignment with the streamwise direction resulting in limited fiber-wall interaction even when the ratio of fiber length to wall-normal distance is smaller than unity. Upon approaching the wall, fiber rotation rates strongly increased. In the wall-normal plane, in-plane fiber rotation rates as a function of wall-normal position were the same for both fiber types. However in wall-parallel planes, in-plane rotation rates of the shorter fibers were higher than those of the longer ones in the buffer layer and vice versa in the wake region. Measured mean-squared fiber tumbling rates strongly increased in the buffer layer for both fiber types, while they remained nearly constant in the log layer and the wake region. A clear length effect was apparent, and the longest fibers consistently tumbled at a higher rate than the shorter ones, surmised to be the result of their interaction with more energetic, larger turbulence structures.

I. INTRODUCTION

The interaction between particles and turbulent boundary layers occurs across a wide range of applications, ranging from dust storms, to chemical plants, to particle deposition within the human body. While much research has focused on spherical particles, nonspherical ones have received considerably less attention. Of particular interest is the interaction between elongated, axisymmetric particles such as fibers and turbulent flows [1]. Understanding their orientation dynamics is essential to control paper quality [2], fabricate composite materials [3], and predict atmospheric particle dispersion [4,5], amongst others.

---

*rene@technion.ac.il

In a fully developed turbulent boundary layer, several regions can be distinguished, each showing distinct turbulence characteristics. Closest to the wall, the viscous sublayer (viscosity dominated) extends up to $y^+(=yu_\tau/\nu) \approx 5$, where y denotes the wall-normal distance and the superscript "+" denotes normalization by inner wall parameters, i.e., the friction velocity, u_τ, and the kinematic fluid viscosity, ν. Further away from the wall ($y^+ \gtrsim 30$), a layer that is characterized by a logarithmic velocity profile (hereafter called the "log layer") develops (inertia dominated); its extent depends on the Reynolds number. The log layer and the viscous sublayer are "bridged" by the buffer layer ($5 < y^+ \lesssim 30$) where both viscous and inertial effects are important. Beyond the log layer a "wake region" develops in the outer layer of the boundary layer [6]. The above, well-accepted description is based on ensemble averaged statistics. However, instantaneous "snapshots" of turbulent boundary layers indicate that they are populated by "coherent structures" that govern momentum, mass, and heat transfer [7,8]. For example, in particle-laden flows, they are responsible for much of the particle transport towards and away from the wall through the action of "sweeps" and "ejections", respectively [9,10]. Furthermore, "trains" of self-generating coherent structures bound low-speed streaks in which particles tend to agglomerate, and preferentially segregate [11,12].

The two main parameters governing the response of a fiber to changes in the surrounding flow are its length and inertia. The former can be characterized by its aspect ratio, $\beta = L/D$, where L and D denote the fiber's length and diameter, respectively [13]. However, close to walls, the ratio, L/y, becomes important, and when $L/y > 1$ fiber dynamics are constrained by wall proximity [14]. The latter is characterized by the Stokes number, $\mathrm{St} = \tau/\tau_v$, which quantifies inertial effects and is defined as the ratio between the fiber response time, τ, and a suitable flow time scale such as the viscous time scale, $\tau_v = \nu/u_\tau^2$. The latter is convenient in wall-bounded flows as its value does not change as a function of wall-normal distance, in contrast to the Kolmogorov time scale.

Analytical solutions for axisymmetric cylindrical bodies such as fibers exist under Stokes flow assumptions [15]. They apply to fibers in turbulent flows as long as St and the fiber Reynolds number, $\mathrm{Re}_L = |\boldsymbol{U}_r|L/(2\nu)$, are much less than unity; $|\boldsymbol{U}_r|$ denotes the magnitude of the fiber translational velocity vector (vectors are denoted in bold typeface) relative to the flow. In addition, L must be small enough to assume simple shear. Note that Re_L is based on $L/2$ that can be considered as the flow scale responsible for exerting torque on the fiber [16].

Fiber orientation depends on the relative importance of (i) orienting factors, such as velocity gradients and external forcing/torques, and (ii) randomizing factors such as Brownian motion and turbulence [16–23]. Fiber dynamics at dilute volume fractions are governed by the history of velocity gradients that fibers experience along their trajectories [24]. In a wall-bounded turbulent flow, Zhao and Andersson [25] and Jie *et al.* [26] showed that inertialess spheroids align with the direction of the Lagrangian stretching that near the wall coincides with the streamwise direction. Several numerical simulations [27–29] showed that preferential alignment with the direction of mean shear increases with increasing β and decreases with increasing St. At the channel centerline, due to small mean velocity gradients, fibers are randomly oriented. Furthermore, it was suggested by Marchioli *et al.* [30] that fiber preferential alignment is imposed during fiber migration towards the wall by sweeps.

While many numerical simulations on fiber translation and rotation in turbulent boundary layers have been published, there is a severe lack of experimental data. Numerical simulations incorporating one-way [27,29–32], two-way [33], and four-way coupling [34] commonly modeled fibers using the point-particle approach. In this approach, the fiber length is taken much smaller than the Kolmogorov length scale [35,36], an assumption often violated in actual practical applications. Using this approach, numerical simulations [27,29,37] showed that β hardly affects clustering and preferential segregation, that are inertia dominated. However, high aspect ratio fibers deposited at increased rates. In and beyond the log layer, both inertial and length effects play a minor role [29].

Fiber rotational motion can be split up into "spinning" and "tumbling," where the former describes rotation about its major axis and the latter describes rotation about its minor axes. Fiber rotation depends on several parameters such as St, β, L/y, and fiber orientation with respect to the direction of Lagrangian stretching. A comprehensive direct numerical simulation study of the

rotation rate of prolate spheroids (resembling fibers) in a turbulent channel flow was performed by Zhao *et al.* [32,38]. Their results indicated that at the channel's center spinning and tumbling [1] were similar as observed in isotropic turbulence. In contrast, in the buffer layer, the rotational motion was affected by both mean shear and anisotropic fluid vorticity. The difference in rotational dynamics at the channel center and near the wall was the result of preferential orientation due to the action of coherent near-wall vortex structures as shown by Yang *et al.* [39]. Furthermore, rotational and translational fiber dynamics became decoupled with increasing fiber length ($\beta \geqslant 10$) [30].

As mentioned before, few experimental studies on fiber dynamics in wall-bounded flows have been published. Holm and Söderberg [40] quantified the effect of laminar simple shear flow on fiber orientation close to a solid boundary and showed that low aspect ratio fibers oriented themselves perpendicular to the streamwise flow direction while exhibiting a rolling-sliding motion in agreement with Gavze and Shapiro [41]. With increasing aspect ratio and concentration, fibers oriented themselves with the streamwise flow direction [40]. Measurements by Bernstein and Shapiro [17] at the center of a turbulent pipe flow showed that for laminar flow glass fibers aligned with the streamwise flow direction while they were randomly distributed in turbulent flow, in agreement with numerical simulations [42]. Capone and Romano [43] measured the fiber orientation in a turbulent channel flow with a backward facing step. Their results also indicated that the fibers were aligned with the mean flow direction except in the high shear layer downstream of the backward step where fibers were orientated with the maximum shear direction. Most relevant to the present paper are the experiments by Hoseini *et al.* [14], who investigated finite-size effects on rotational and translational fiber motion ($St < 1$) in a wall-bounded turbulent flow using two-dimensional particle image velocimetry (PIV) and particle tracking velocimetry. Their measurements were performed in three wall-parallel planes located at $y^+ = 14$, 43, and 72. Probability density functions (PDF's) of fiber streamwise velocities were in agreement with numerical simulations [27], except at $y^+ = 14$, where a bimodal distribution was obtained, most distinct for the longest aspect ratio fibers. They showed that the dynamic behavior of long fibers ($L/y > 1$) was severely constrained by wall proximity, while short fibers ($L/y < 1$) preferentially segregated in low-speed streaks. In the log layer ($L/y \ll 1$), translational velocity statistics were unaffected by L. Neither of the above experiments measured the three-dimensional (3D) fiber orientation or the tumbling rate in a wall-bounded flow.

The goal of the present paper is to measure length effects on the 3D orientation and the translation and rotation dynamics of fibers in the vicinity of the wall in a turbulent channel flow. Two different nylon fiber types having similar St (0.22 and 0.34) but different mean lengths (1594 and 2917 μm) were investigated. The measurements were performed using two-orthogonal view, digital holographic cinematography similar to that previously successfully developed and employed by our research group in isotropic turbulence [22,23]. This technique resolves the instantaneous 3D fiber orientations and their tumbling rates. A short description of the experimental setup and methodology is given in Sec. II. Results are presented in Sec. III, and a summary and conclusions are provided in Sec. IV.

II. EXPERIMENTAL SETUP AND METHODOLOGY

Experiments were performed in a horizontal, closed-loop water tunnel (50×50 mm^2 internal cross-section) consisting of a frequency controlled centrifugal pump, a magnetic flow meter, an inlet diffuser, and a 9:1 contraction section. The test section walls were made of glass to ensure optical access from all sides. For a detailed description of the experimental facility, the reader is referred to van Hout *et al.* [44]. Access into the test section was provided by an internally flush mounted acrylic lid on top of the test section. The bulk water velocity was $U_m = 0.3$ m/s, corresponding to a Reynolds number, $Re_h = U_m h/\nu = 7353$, where h denotes the channel half height and ν the kinematic water viscosity at 25 °C. The uncertainty in the bulk flow velocity was less than 2% [10]. The flow conditions were the same as those reported by van Hout [10,45], in the same facility, and the wall friction velocity was $u_\tau = 0.0174$ m/s ($Re_\tau = u_\tau h/\nu = 435$). In order to trip the boundary
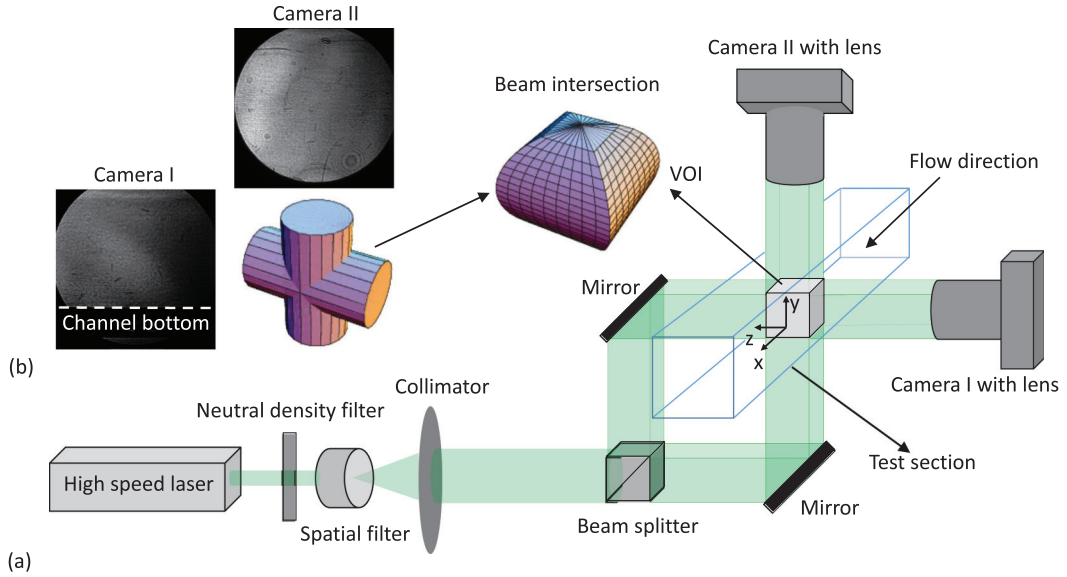
FIG. 1. (a) Schematic layout of the experimental facility (not to scale) including part of the test section, the setup of the two-orthogonal view digital holography system, the VOI, and the employed coordinate system. (b) Intersection of the two perpendicular illumination beams and actual shape of the VOI. Also depicted are examples of actual recorded holograms by both cameras.

layer and attain fully developed turbulent flow at the measurement position, a zigzag boundary layer trip was attached to the internal walls at the entrance of the channel [46]. Measurements were performed at a distance of 1.3 m ($52h$) from the channel entrance, where the turbulent flow was fully developed [10,45].

The 3D fiber orientation and translation dynamics were measured using two-orthogonal view, digital inline Fraunhofer holographic cinematography. The system, schematically depicted in Fig. 1, was comprised of a high-speed laser (CrystaLaser, 10-μJ/pulse at 10 kHz), two high-speed complementary metal-oxide semiconductor cameras (Photron Ultima APX, 1024×1024 pixels at 2 kHz) equipped with 105-mm lenses (Nikon, MicroNikkor), a neutral density filter and a spatial filter (aspherical focusing lens and 10-μm pinhole), a collimating lens (200-mm focal length), a beam splitter, and two mirrors to direct the laser beams to the cameras. The system was carefully calibrated in order to quantify the magnifications in the illumination directions as a result of the difference in refractive indices of the media that the laser beams traversed [47,48]. The measured magnifications in the illumination directions were 1.37, i.e., within 3% of the theoretical value of 1.33. In-plane magnifications were absent and the spatial measurement resolution was 33 μm/pixel. The intersection between the two collimated beams comprised the volume of interest (VOI, approximately $35 \times 25 \times 35$ mm^3, see Fig. 1). Note that the VOI spanned half of the tunnel height and its size was chosen to ensure sufficient spatial resolution for the detection and reconstruction of the fibers. However, since lenses were used, the actual VOI was the intersection of two perpendicular cylindrical beams as schematically illustrated in Fig. 1(b). Furthermore, due to chamfers of the test section walls, data below $y^+ = 14$ were not resolved. The employed coordinate system is depicted in Fig. 1(a) where x, y, and z denote the streamwise, wall-normal, and transverse directions, respectively. The corresponding streamwise water velocity is denoted by U_x.

Two different batches of rigid, nylon fibers (density $\rho = 1150$ kg/m^3; Claremont Flock, USA) having similar St but different β and $\overline{L}^+(=\overline{L}u_\tau/\nu)$ were selected. An overbar denotes ensemble averaging. The fibers can be considered straight, and their length and diameter distributions were

TABLE I. Summary of fiber characteristics.

Type	Symbol	$\overline{L}(\mu m)$	$\overline{D}(\mu m)$	β	$\overline{L}^+$	τ (ms)	St	V_s (m/s)
t1	△	1594 ± 174	52 ± 3.62	30.7 ± 3.9	27.7 ± 3	0.7 ± 0.1	0.22 ± 0.03	-1.1×10^{-3}
t2	◇	2917 ± 242	62 ± 5.5	47.0 ± 5.7	50.8 ± 4.2	1.12 ± 0.2	0.34 ± 0.06	-1.7×10^{-3}

presented by Kuperman *et al.* [23]. Fiber characteristics pertinent to the present paper are summarized in Table I; subscripts "t1" and "t2" denote fiber types 1 and 2, respectively.

The fiber's translational response time for randomly oriented fibers in Stokes flow (Re $\ll$ 1) depends on the aspect ratio and can be determined using the following expression [37,49]:

$$\tau = \frac{\rho D^2}{18\mu} \beta \frac{\ln(\beta + \sqrt{\beta^2 - 1})}{\sqrt{\beta^2 - 1}}, \tag{1}$$

where μ is the fluid dynamic viscosity. Calculated fiber response times and associated Stokes numbers are summarized in Table I. Note that the fiber's rotational response time can be assumed to be smaller than the translational one [1,32,50]. As can be seen in Table I, both fiber types have St <1, and the small difference in Stokes number between them is expected to have a negligible effect on their rotational and translational dynamics [31]. However, fiber lengths differ by almost a factor of 2 and length effects are expected to have an impact, especially in the vicinity of the wall. The fiber's settling velocities under quiescent conditions, V_s, determined using the expression given by Herzhaft and Guazzelli [51], are also given in Table I. Note that it was assumed that fibers settle with their major axes perpendicular to gravity (see also [22,23]). In case the major fiber axis is aligned with gravity, fibers may settle twice as fast [52,53].

Prior to the start of the measurements, the fibers were mixed in a large water tank and the flow was recirculated through the system until they were thoroughly mixed with the flow. Note that gravity did not affect the fibers' wall-normal distribution significantly, and fiber number densities remained approximately constant with wall-normal distance except for the immediate near-wall region where number densities decreased significantly (not shown). For each investigated fiber type, data sets were acquired at 500 Hz corresponding to $\Delta t^+ = 0.61$ between frames. A single data set was comprised of 4096 holograms (2048 from each camera) limited by available on-camera memory. In order to ensure converged statistics, more than 36 000 fiber tracks were collected for each fiber type over multiple data sets ($\approx$65 sets), resulting in a total number of detected instantaneous fiber instances that ranged from 300 000 to 500 000 depending on the fiber type. Average fiber volume fractions (based on the reconstructed holograms) ranged between 10^{-8} and 10^{-7}, i.e., one-way coupling can be assumed [54].

Holograms of the fibers in suspension were recorded at the camera sensors as a result of the interference between the diffracted object beams (from the fibers) and the undiffracted reference beam [47]. Examples are shown in Fig. 1(b) for both cameras. Acquired holograms were digitally reconstructed by solving the Fresnell-Kirchhoff integral [55–57] using the fast Fourier transform [58]. In order to improve the signal to noise ratio, recorded holograms were normalized by the first hologram in the data set, subsequently averaged, and subtracted from all holograms in the data set. This procedure alleviated spatial nonuniformities in light intensity and improved fiber tracking along frames. Data processing involved a coarse reconstruction scheme for each camera separately [48] in which all fibers within the VOI were detected without determining their accurate in-focus positions (for camera I, this is along the z direction, Fig. 1). Reconstructions were binarized and at each time instant collapsed onto a single binary image containing the detected fibers. Based on these binary images, the centroid positions and in-plane fiber orientation angles were determined for each camera separately (for more details see [22]).

The employed coordinate systems and definitions of the fiber orientation angles are schematically depicted in Fig. 2 together with the planar field of views of cameras I and II. Subscripts "I" and "II"
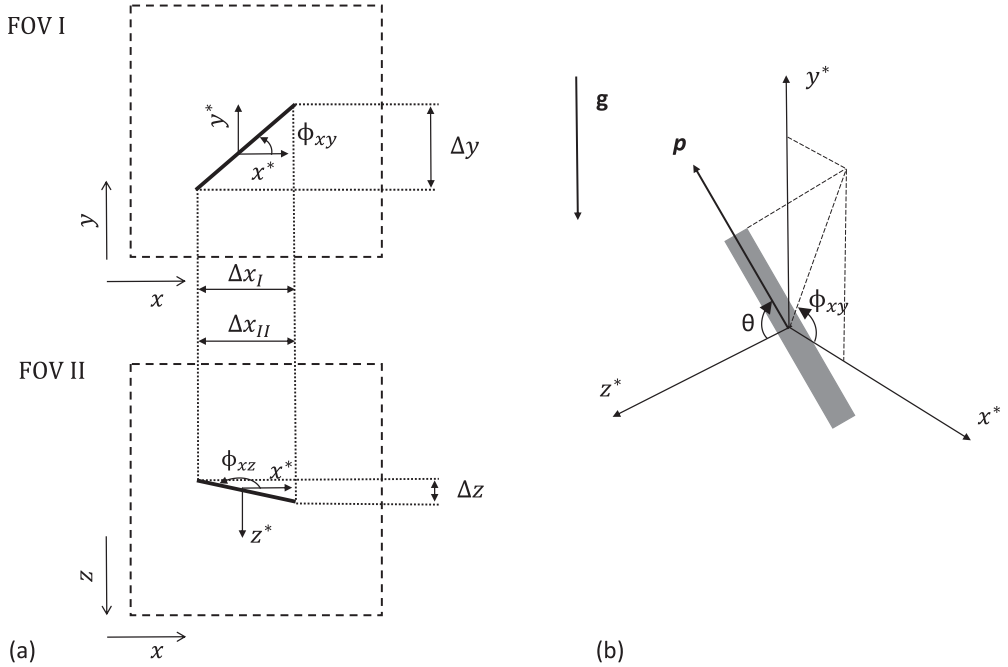
FIG. 2. (a) Definition of the fiber and associated coordinate systems projected onto the fields of view of cameras I and II (not to scale). (b) Definition of fiber polar angle, azimuthal angle, and unit orientation vector in a comoving coordinate system.

denote cameras I and II, respectively, and Δx, Δy, and Δz denote the projected, measured fiber lengths onto the corresponding x, y, and z axes. The in-plane angles ϕ_{xy} and ϕ_{xz} denote the fiber angles in the x-y and x-z planes, respectively, that were determined directly from the reconstructed holograms. The fiber polar angle, θ, defined in a spherical coordinate system is also depicted in Fig. 2(b). The x^*, y^*, and z^* axes are associated with a nonrotating, comoving coordinate system with origin at the fiber's centroid.

Three-dimensional fiber positions and orientations were determined by combining the measured fiber positions and orientations from cameras I and II, while 3D fiber tracks were constructed by matching the in-plane tracks through their common x coordinate [see Fig. 2(a)] similar as described in Sabban *et al.* [22]. The instantaneous fiber length and polar angle were calculated as $L = \sqrt{\Delta x_I^2 + \Delta y^2 + \Delta z^2}$ and $\theta = \cos^{-1}(\frac{\Delta z}{L})$, respectively. In order to discard spurious noise, only fiber tracks longer than five instances were considered. The reconstructed VOI was divided into several subvolumes spanning the buffer layer, the log layer, and the wake region of the turbulent boundary layer. Translational fiber velocities with components V_x, V_y, and V_z in the corresponding x, y, and z directions were calculated by applying a centered difference scheme to the filtered (using a smoothing spline) centroid positions along a fiber track. Forward and backward schemes were applied at the ends of the track. Similarly, in-plane rotation rates, $\dot{\phi}_{xy}$ and $\dot{\phi}_{xz}$, were determined based on the change in in-plane orientations along tracks.

In order to describe the fiber's 3D orientation we use its unit orientation vector defined by [19]:

$$\boldsymbol{p} = \begin{bmatrix} \cos\phi_{xy}\sin\theta \\ \sin\phi_{xy}\sin\theta \\ \cos\theta \end{bmatrix} \begin{bmatrix} \hat{j} \\ \hat{k} \\ \hat{l} \end{bmatrix}, \tag{2}$$
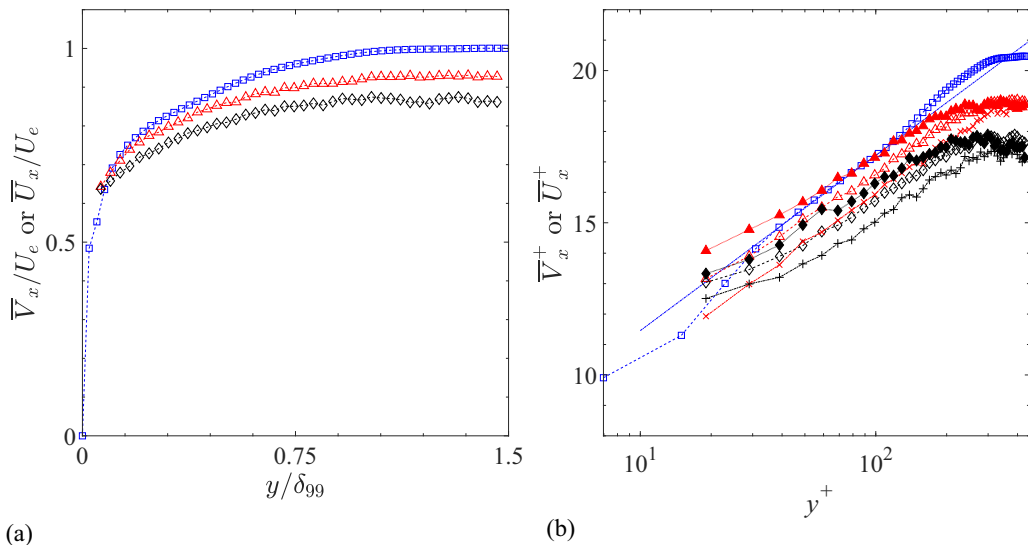
FIG. 3. Mean, streamwise translational fiber centroid velocities and fluid velocities plotted in (a) outer scaling and (b) inner wall scaling as a function of wall-normal distance. Fluid velocity: $\square$ $\overline{U}_x$ [45]. Present data: $\overline{V}_x$. Fiber types: $\triangle$ t1, $\diamond$ t2. Conditionally sampled data set: "ascending" fibers, $\times$ t1, $+$ t2; "descending" fibers, (filled triangle) t1, (filled diamond) t2. The logarithmic velocity profile, $u^+ = \kappa^{-1}\ln y^+ + B$, is displayed [dash-dotted line in (b)] with the von Kármán constant, $\kappa = 0.4$, and the intercept $B = 5.7$.

where $\hat{j}, \hat{k},$ and $\hat{l}$ are unit vectors in the x, y, and z directions, respectively. The fiber's rotation (or tumbling) rate is then given by

$$\dot{\boldsymbol{p}} = \dot{\phi}_{xy}\sin\theta\hat{\phi}_{xy} + \dot{\theta}\hat{\theta}, \tag{3}$$

where $\hat{\phi}_{xy} = [-\sin\phi_{xy}; \cos\phi_{xy}; 0]$ and $\hat{\theta} = [\cos\phi_{xy}\cos\theta; \sin\phi_{xy}\cos\theta; -\sin\theta]$ are the unit vectors and $\dot{\phi}_{xy}$ and $\dot{\theta}$ are the fiber in-plane and polar angular velocities, respectively. The components of $\dot{\boldsymbol{p}}$ are denoted by $\dot{p}_i$.

Uncertainties were determined as the standard error of the distribution employing a 95% confidence interval. However, since the present data along fiber tracks were statistically dependent, the ensemble size was taken as the relevant number of independent fiber tracks.

III. RESULTS

A. Translational fiber velocities

The measured ensemble averaged, streamwise fiber centroid velocities, $\overline{V}_x$, are depicted in Fig. 3 for both fiber types together with the mean streamwise fluid velocity, $\overline{U}_x$ [45]. Instantaneous fiber velocities were ensemble averaged as follows. First, all instantaneous fiber instances were binned into wall-parallel "slabs" having a wall-normal thickness of $\Delta y^+ = 10$. Subsequently, for each bin the ensemble average was calculated. Note that for this bin size the average number of independent samples within each bin exceeded 900 fibers, while the number of fiber instances in each bin was of the order of 10 000. Note that the bin closest to the wall is centered at $y^+ = 19$. The data are depicted both in outer wall [Fig. 3(a)] and inner wall scaling [Fig. 3(b)]. Values of $\overline{U}_x$ attained a constant value farthest from the wall, $U_e = 0.356 \pm 0.003$ m/s. The boundary layer thickness, δ_{99}, defined as the distance from the wall where $\overline{U}_x = 0.99\overline{U}_e$, was determined as $\delta_{99} = 16.9 \pm 1.4$ mm. Based on the distribution of $\overline{U}_x$, the displacement and momentum thicknesses were $\delta^* = 2.48$ mm and $\theta = 1.73$ mm, respectively. The associated shape factor is $H = \delta^*/\theta = 1.44$, i.e., typical of a

turbulent boundary layer. The velocity profile of $\overline{U}_x^+$ versus y^+ depicted in Fig. 3(b) indicates that a logarithmic layer is attained at $30 < y^+ < 150$. For $y^+ > 150$, a wake region can be observed while the remaining data close to the wall are within the buffer layer. Comparing the mean fiber centroid velocities to the fluid ones shows that away from the wall (beyond the buffer layer, $y^+ > 30$) fibers move on average slower than the fluid. This is true for both fiber types. However, type 2 fibers (hereafter termed t2 fibers), that are almost twice as long as type 1 (hereafter termed t1 fibers), have lower $\overline{V}_x$. Only in the bin closest to the wall, the streamwise velocities of both fiber types are almost equal and exceed those of the fluid as will be further discussed in the following. The lower streamwise velocities of t2 fibers compared to those of t1 can be attributed to increased drag exerted on the longer t2 fibers [52] due to their increased surface area. In addition, the drag force per unit length of a cylinder in uniform flow depends on its orientation with respect to the surrounding flow, and is minimal when a fiber has its major axis aligned with the relative velocity vector between the fiber and the flow (see also [22,53]). Since in a channel flow the relative velocity vector is governed by the streamwise velocity, the drag force will be minimum when the fibers preferentially align with the streamwise direction. We will show in Sec. III B that fiber alignment with the streamwise direction occurs close to the wall and is more pronounced for t1 fibers than for the longer t2 fibers. Therefore, the combination of preferential alignment and shorter fiber length leads to reduced drag acting on t1 fibers compared to the t2 fibers.

As mentioned before, closest to the wall [$y^+ < 24$, Fig. 3(b)], fiber velocities exceed the fluid ones. While this may seem odd at first, excess velocities of particles in the near-wall region of a turbulent boundary layer have been reported for both finite-size spheres [59–61] and nonspherical particles [34,62,63], and are the result of preferential accumulation in high-speed streaks. Do-Quang *et al.* [63] performed direct numerical simulations accounting for the finite size of three fiber types ($\overline{L}^+ = 3.2$, 9.6, and 24) with relatively low inertia (St < 3). They showed that $\overline{V}_x^+ > \overline{U}_x^+$ in the near-wall region ($y^+ < 30$). The "excess" velocity, ($\overline{V}_x^+ - \overline{U}_x^+$), increased with increasing fiber length. Note that, in contrast, numerical simulations implementing the point-particle approach [27,29] showed preferential accumulation in low-speed streaks except for high inertia (St $= 30$) prolate spheroids that displayed an excess velocity in the viscous sublayer. The results of Do-Quang *et al.* [63] were corroborated by Zhu *et al.* [62], who performed interface resolved numerical simulations of neutrally buoyant, spheroidal particles in a turbulent channel flow and showed that in the near-wall region ($y^+ < 60$) $\overline{V}_x^+ > \overline{U}_x^+$.

Experimental validation of excess velocities of fibers in wall-bounded turbulent flows is nearly completely lacking. As far as we are aware, the only measurements that report $\overline{V}_x^+ > \overline{U}_x^+$ are those in the Ph.D. dissertation by Hoseini [64] for fibers having an aspect ratio of $\beta = 28$ at wall-normal positions of $y^+ = 14$ and 43. For smaller aspect ratio fibers, $\overline{V}_x^+ < \overline{U}_x^+$ were reported. Note that in the present measurements fiber aspect ratios exceed $\beta = 28$ (see Table I), and our results that are at higher Re$_\tau$ agree with those by Hoseini [64].

In order to investigate the effect of sweeps and ejections, V_x were conditionally sampled and divided into sets of "ascending" fibers for which $V_y > 5|V_s|$ and "descending" fibers for which $V_y < -5|V_s|$ [Fig. 3(b)]. In the near-wall region, the streamwise fiber velocities of descending fibers exceed those of ascending ones in agreement with the effect of sweeps and ejections [65]. However, this effect fades away with increasing wall-normal distance [$y^+ > 300$, Fig. 3(b)].

To get a better idea of the distribution of the fiber velocities in different regions of the turbulent boundary layer, PDF's of V_x^+, V_y^+, and V_z^+ are presented in Fig. 4. The data depicted in Fig. 4 were binned across different "slabs" spanning $14 < y^+ \leqslant 30$ (top row in Fig. 4, buffer layer), $30 < y^+ \leqslant 150$ (middle row in Fig. 4, log layer), and $150 < y^+ \leqslant 430$ (bottom row in Fig. 4, wake region). Associated wall-normal profiles of the third ("skewness") and fourth ("kurtosis") order moments calculated for data bins with $\Delta y^+ = 10$ are presented in Fig. 5. Note that the higher order moments showed more scatter and to more clearly present trends, outliers in the tails of the velocity
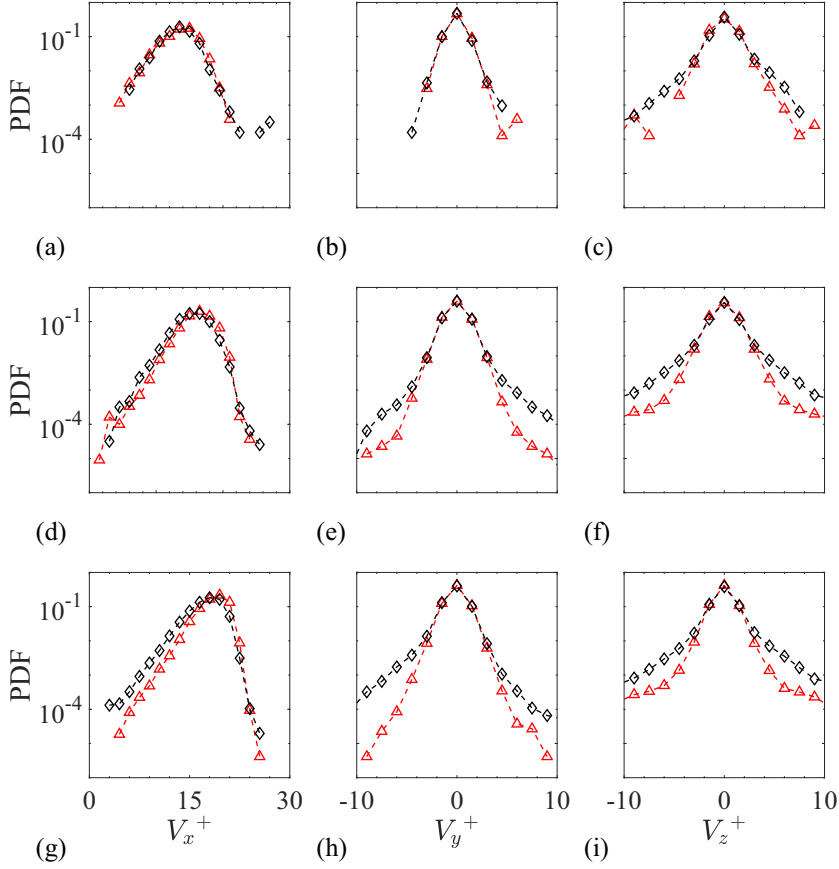
FIG. 4. Probability density functions of V_x^+ (left column), V_y^+ (middle column), and V_z^+ (right column) at different wall-normal positions. Data were binned in slabs extending between (a)–(c) $14 < y^+ \leqslant 30$ (buffer layer), (d)–(f) $30 < y^+ \leqslant 150$ (log layer), and (g)–(i) $150 < y^+ \leqslant 430$ (wake region). Fiber types: △ t1, ◇ t2.

distributions were removed prior to calculating the skewness and kurtosis, and subsequently profiles were smoothed using a robust linear regression method ("rlowess," MATLAB).

It can be observed that the shape of the PDF's of V_x^+ (left column in Fig. 4) changes upon moving away from the wall and becomes increasingly negatively skewed [see also Fig. 5(a)], in agreement with the measurements by Hoseini *et al.* [14]. In contrast, skewness values of the PDF's of V_y^+ and V_z^+ are close to zero [characteristic of a normal distribution, see Figs. 5(b) and 5(c)], except for the PDF's of $V_{y,t2}^+$ [Fig. 5(b)] the skewness of which changes from being positive near the wall to being negative farther away from it, indicating high probabilities of rare events of fast upward moving t2 fibers [Fig. 4(e)] or fast downward moving t2 fibers [Fig. 4(h)]. The reason for this "asymmetry" is not completely clear at this point but may be related to differences in the turbulence activity in the buffer layer and the wake region that become significant with increasing fiber length.

Closest to the wall, inside the buffer layer ($14 < y^+ \leqslant 30$, top row in Fig. 4), the PDF's of V_x^+ and V_y^+ for both fiber types collapse. Note that proximity to the wall is expected to affect fiber motion [14]. However, in the present paper, the smallest wall-normal position for which fibers were detected was $y^+ = 14$. Assuming that the length scale dictating wall interaction is $\overline{L}^+/2$, we can conclude that only t2 fibers ($\overline{L}_{t2}^+/2 \approx 25$) are expected to be affected by wall interactions. However, wall proximity seems to have the same effect for both fiber types, irrespective of length differences,
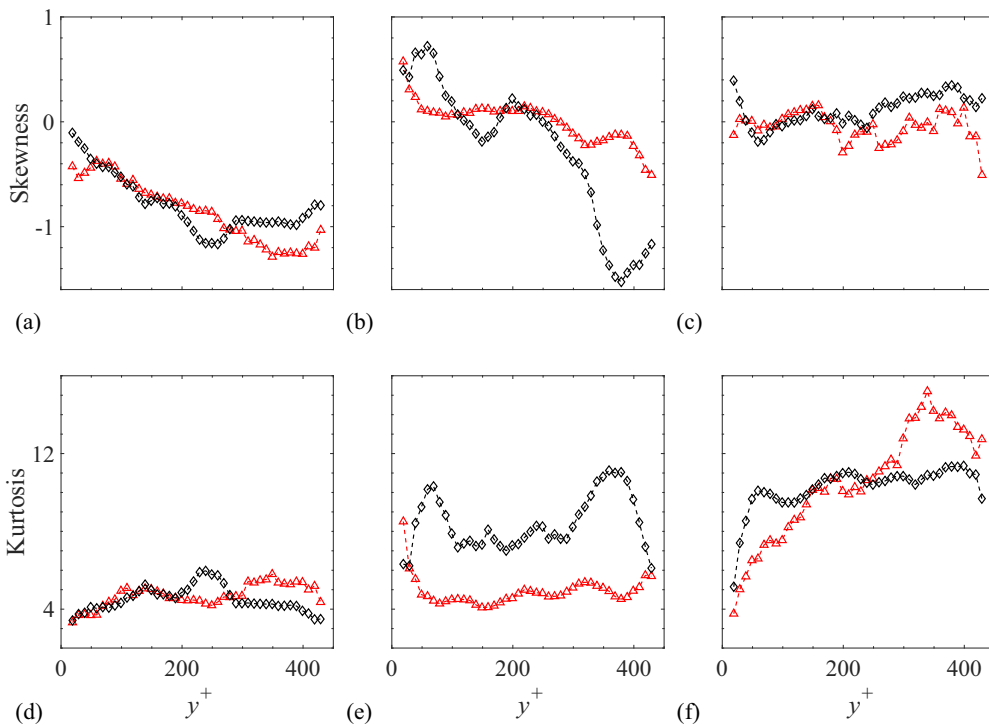
FIG. 5. Skewness (upper row) and kurtosis (bottom row) of the PDF's of instantaneous fiber velocities plotted as a function of wall-normal distance (bin size $\Delta y^+ = 10$). Fiber types: △ t1, ◇ t2. Skewness and kurtosis values of 0 and 3, respectively, correspond to those characterizing a normal distribution. Left column, V_x^+; middle column, V_y^+; and right column, V_z^+.

as indicated by the collapse of the PDF's of V_x^+ and V_y^+ for both fiber types. This is the result of the strong fiber alignment with the streamwise direction in the proximity of the wall which will be discussed in the next section. In all other regions of the turbulent boundary layer, the PDF's do not collapse. PDF's of $V_{x,t2}^+$ become slightly shifted towards lower velocities compared to t1 fibers, in agreement with their lower $\overline{V}_x^+$ (Fig. 3). The most striking difference between both fiber types appears in the PDF's of V_y^+ and V_z^+ (middle and right columns in Fig. 4). It is clear that for t2 fibers relatively rare high magnitude velocities ("tails") occur at higher probabilities than for t1 fibers, in agreement with the higher kurtosis values depicted in Figs. 5(e) and 5(f). Note that a turbulent boundary layer is populated by hairpinlike vortices that may be "broken up" into longitudinal "legs" and spanwise "arches" that may lead to significant wall-normal and transverse forcing. Since fiber motion is affected by turbulence scales of the order of the fiber length [23,66], these high probabilities are associated with the length difference between t1 and t2 fibers. The latter are almost twice as long as the former, and are affected by larger, more energetic turbulence structures that reside in a wall-bounded flow (e.g., coherent hairpinlike structures), leading to more extreme events for the t2 fibers. In contrast, streamwise motion of the fibers is dictated by the drag force acting on them, leading to lower V_x^+ for t2 fibers compared to t1 fibers, as previously discussed.

B. Fiber orientation

In this section, the orientation statistics of the investigated fibers are presented. First, fiber in-plane orientations in the x-y and x-z planes that were directly determined from the reconstructed holograms (see Sec. II) will be discussed. Subsequently, the calculated direction cosines will be
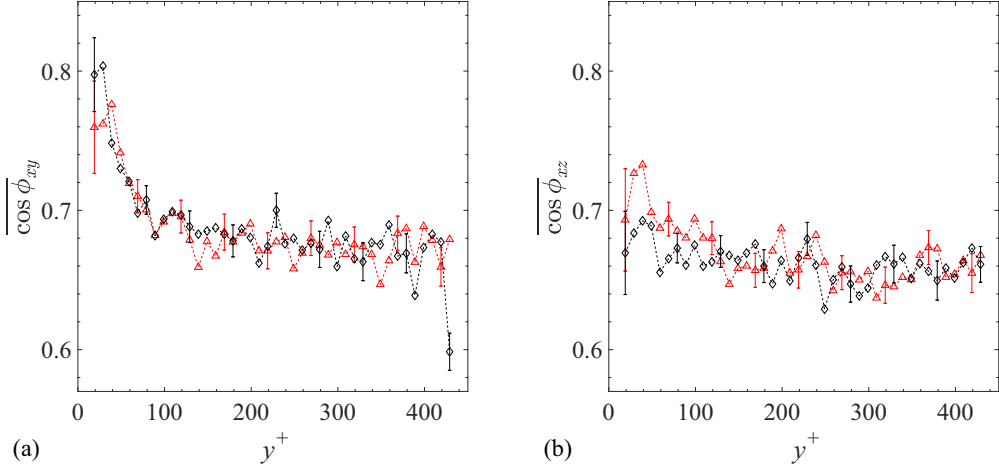
FIG. 6. Ensemble averaged cosines of the in-plane fiber angles as a function of wall-normal distance: (a) ϕ_{xy} and (b) ϕ_{xz}. Fiber types: △ t1, ◇ t2. Representative error bars denote standard errors at 95% confidence intervals.

presented. Note that direction cosines are usually presented in numerical studies while in-plane orientations are more easily obtained in experimental studies, e.g., using a single camera setup as employed by Hoseini *et al.* [14] and Capone and Romano [43].

The ensemble averaged cosines of the fiber in-plane projected angles, $\overline{\cos \phi_{xy}}$ and $\overline{\cos \phi_{xz}}$, are depicted with increasing wall-normal position in Fig. 6 for both investigated fiber types. Note that the x-y and x-z planes correspond to the streamwise and wall-normal and the streamwise and transverse planes, respectively (see Fig. 1). In agreement with numerical simulations [27,29–31,34,37] as well as the few available experiments [14,43], our results indicate that fibers preferentially align with the streamwise direction (Fig. 6). The alignment is strongest in the near-wall region and more pronounced in the x-y plane [Fig. 6(a)]. Values of $\overline{\cos \phi_{xy}}$ strongly peak inside the buffer layer, $y^+ \approx 30$, and reach values of about 0.77 and 0.8 for t1 and t2 fibers, respectively. Closer to the wall ($y^+ < 30$), preferential alignment with the streamwise direction slightly decreases; however, it remains high within our measurement range. Peak values of $\overline{\cos \phi_{xz}}$ [Fig. 6(b)] are lower than those of $\overline{\cos \phi_{xy}}$ close to the wall ($y^+ < 40$), indicating that alignment in the x-z plane with the streamwise direction is slightly less than that in the x-y plane. In all cases, preferential alignment reduces upon moving away from the wall, and beyond $y^+ \approx 80$ plateau values between 0.65 and 0.68 are reached.

Differences in preferential alignment between t1 and t2 fibers are negligible beyond $y^+ \approx 100$, in agreement with numerical studies by Mortensen *et al.* [27] and Marchioli *et al.* [29], who reported that length effects on fiber orientation become negligible away from the wall. On the other hand, close to the wall, the longest t2 fibers ($\overline{L}_2^+ = 50.8$) align better with the streamwise direction in the x-y plane [Fig. 6(a)] than t1 fibers ($\overline{L}_1^+ = 27.7$), but worse in the x-z plane [Fig. 6(b)]. It is surmised that this is the result of the enhanced interaction of the longer t2 fibers with the near-wall coherent structures that have typical transverse spacings of about $100z^+$ units [12]. Therefore, it can be anticipated that the longer fibers are more affected by the transverse, spatially changing flow field resulting in reduced alignment with the streamwise direction in the x-z plane.

PDF's of $2\phi_{xy}/\pi$ and $2\phi_{xz}/\pi$, as well as $\cos \phi_{xy}$ and $\cos \phi_{xz}$, provide more insight into the instantaneous fiber in-plane orientations. Note that PDF's of $2\phi_{xy}/\pi$ depict the actual in-plane angle distributions whereas upon taking the cosine, nonlinearly "distorts" the distributions. The PDF's of both fiber types are plotted in Fig. 7 for different regions in the turbulent boundary layer, i.e., the buffer layer (top row in Fig. 7), the log layer (middle row in Fig. 7), and the wake region (bottom row in Fig. 7). In the log layer [Figs. 7(c) and 7(d)] and the wake region [Figs. 7(e) and 7(f)], PDF's
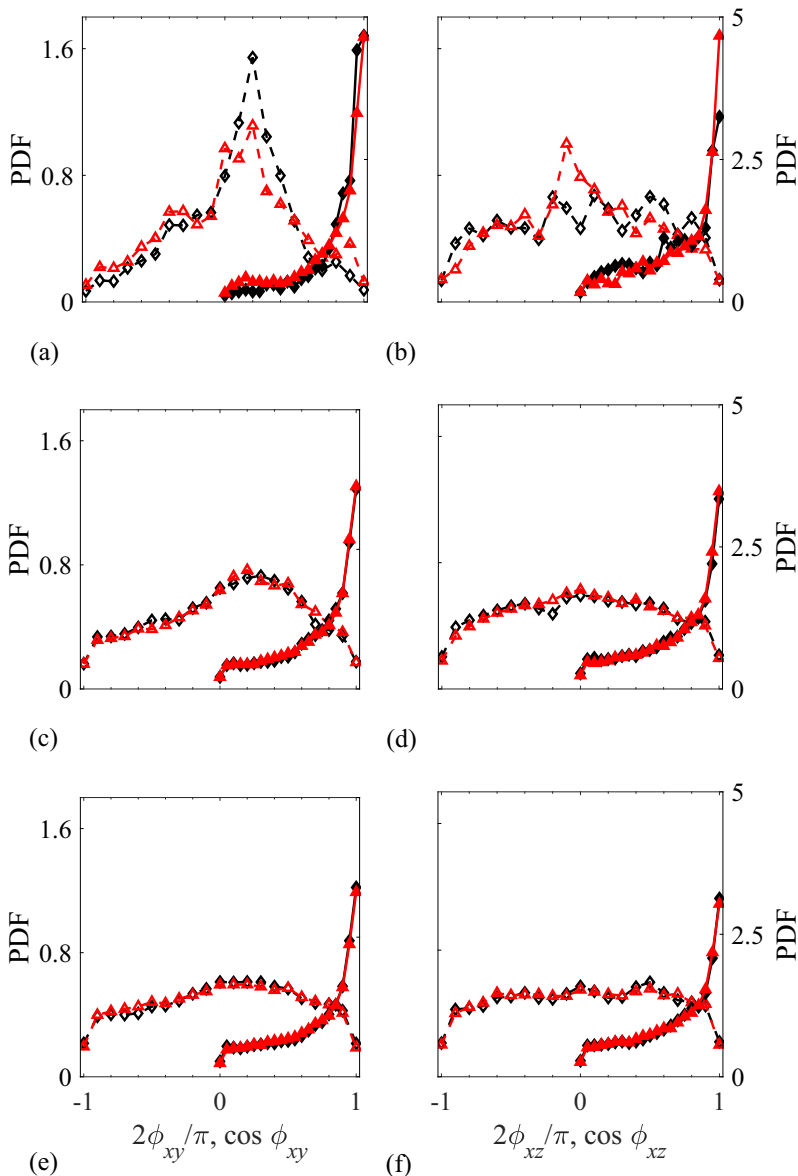
FIG. 7. PDF's of fiber in-plane orientations in different regions of the turbulent boundary layer. Left column, x-y plane; right column, x-z plane. Fiber types: t1 (red), t2 (black). $2\phi_{xy}/\pi$ and $2\phi_{xz}/\pi$ are depicted as open symbols connected by dashed lines (primary y axis); $\cos\phi_{xy}$ and $\cos\phi_{xz}$ are depicted as closed symbols connected by solid lines (secondary y axis). (a), (b) $14 < y^+ \leqslant 30$ (buffer layer). (c), (d) $30 < y^+ \leqslant 150$ (log layer). (e), (f) $150 < y^+ \leqslant 430$ (wake region).

of both fiber types collapse, while in the buffer layer [Figs. 7(a) and 7(b)] they differ mainly in peak values. Within the buffer layer [Figs. 7(a) and 7(b)], PDF's of $2\phi_{xy}/\pi$ [Fig. 7(a)] strongly peak at small positive ϕ_{xy} in agreement with Zhu *et al.* [62]. Peak values are highest for the longest t2 fibers ($\overline{L}_2^+ = 50.8$). Changes in the distribution of the PDF's are most obvious for $2\phi_{xy}/\pi$ (left column in Fig. 7) that become increasingly uniform with increasing distance from the wall (Fig. 7). A similar "flattening" is also observed for PDF's of $2\phi_{xz}/\pi$ (right column in Fig. 7), however, to a lesser
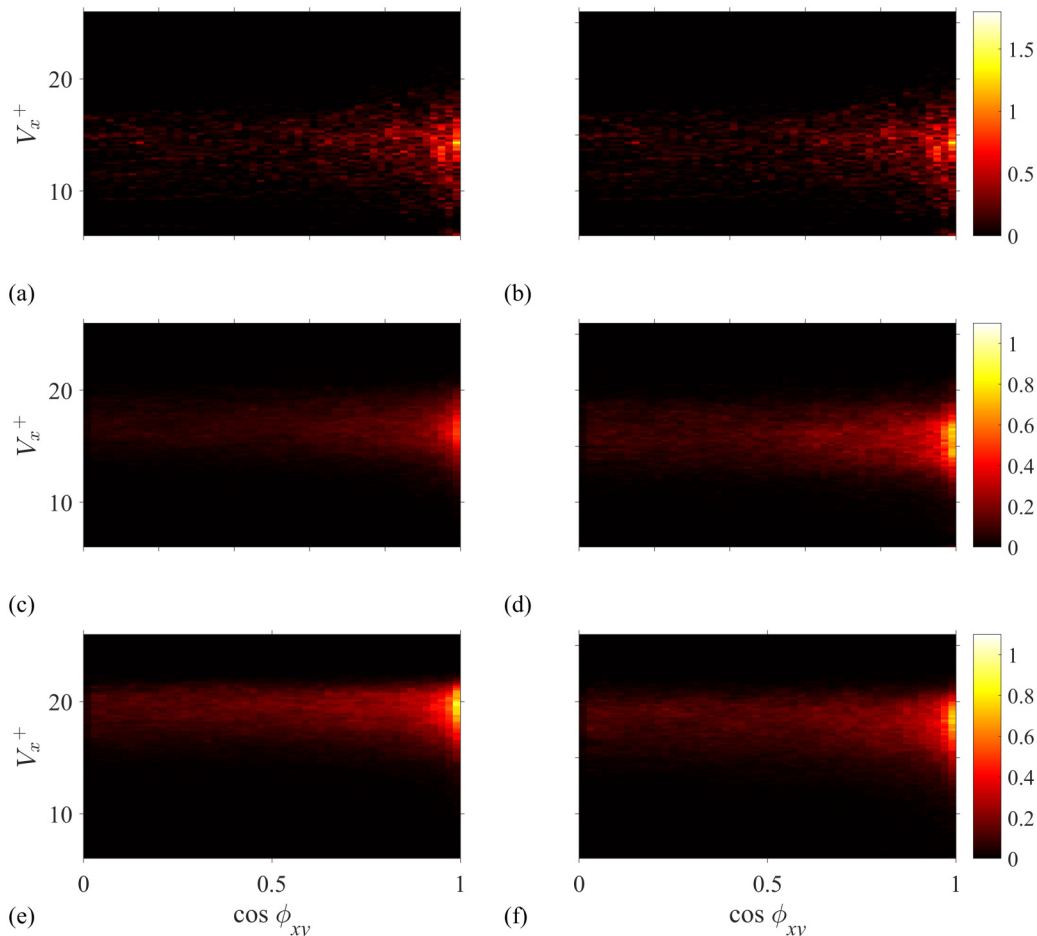
FIG. 8. JPDF's of V_x^+ and $\cos\phi_{xy}$ in different regions of the turbulent boundary layer. (a), (b) $14 < y^+ \leqslant 30$ (buffer layer). (c), (d) $30 < y^+ \leqslant 150$ (log layer). (e), (f) $150 < y^+ \leqslant 430$ (wake region). Fibers: t1 (left column), t2 (right column).

extent. Note that similar trends for ϕ_{xy} were reported by Capone and Romano [43] and attributed to wall proximity constraining possible fiber orientation angles.

The range corresponding to $2\phi_{xy}/\pi < 0.4$ is "condensed" into the range for which $\cos\phi_{xy} > 0.8$ (similarly for ϕ_{xz}), and provides less information on the change in the shape of the PDF's. Furthermore, it obscures the slight asymmetry in $2\phi_{xy}/\pi$ that peaks at small positive angles as mentioned before. Peak values of the PDF's of $\cos\phi_{xy}$ and $\cos\phi_{xz}$ are obtained for $\cos\phi = 1$ in agreement with the numerical simulation of Zhu *et al.* [62], and decrease with increasing distance from the wall as distributions of ϕ_{xy} and ϕ_{xz} flatten.

In order to investigate if there is any correlation between streamwise fiber velocities and their orientations, joint PDF's (JPDF's) of V_x^+ and $\cos\phi_{xy}$ were determined. They are depicted in Fig. 8 for both fiber types within the buffer layer [Figs. 8(a) and 8(b)], the log layer [Figs. 8(c) and 8(d)], and the wake region [Figs. 8(e) and 8(f)]. Similar results were obtained in the JPDF's of V_x^+ and $\cos\phi_{xz}$ (not shown). The experimental results by Hoseini *et al.* [14] indicated that, in particular, relatively slow moving fibers preferentially align with the streamwise direction (only at $y^+ = 14$). Our results (Fig. 8) indicate only a weak dependence of orientation on V_x^+, perhaps due to the fact that our measurement location starts slightly further away from the wall than those of Hoseini *et al.*
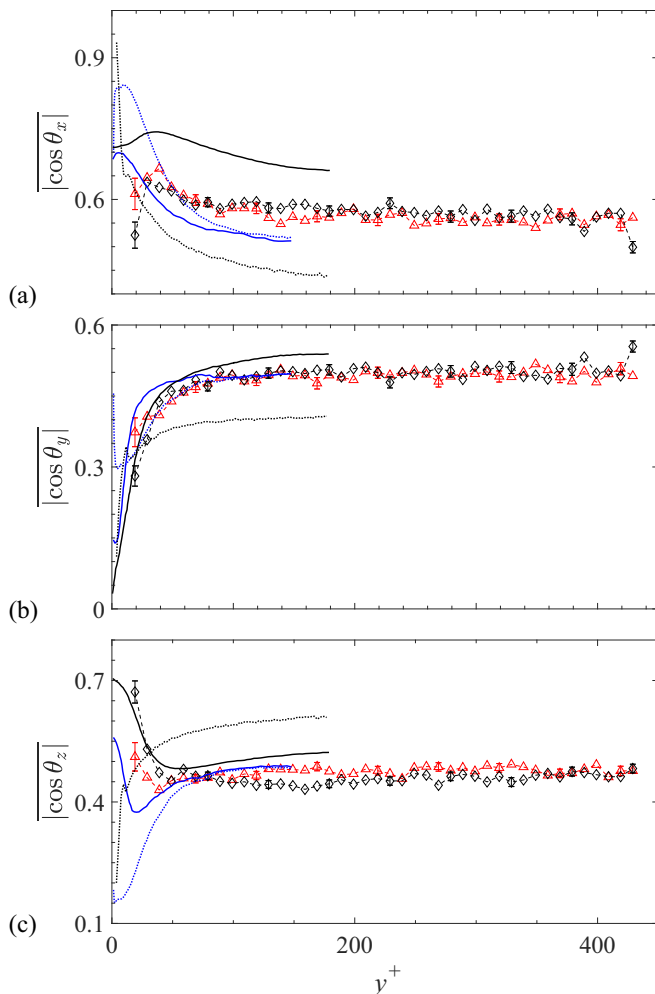
FIG. 9. Ensemble averaged values of the magnitudes of the direction cosines as a function of wall-normal distance. Present results: △ t1, ◇ t2 (bin size $\Delta y^+ = 10$). Representative error bars denote standard errors at 95% confidence intervals. Literature results: Blue solid lines (St = 5, $\beta = 3$, Re$_\tau$ = 150) and blue dotted lines (St = 5, $\beta = 50$, Re$_\tau$ = 150), point-particle approach, one-way coupling [29]. Black solid lines (St = 30, $\beta = 5$, Re$_\tau$ = 180), point-particle approach, strongly coupled simulations [67]. Black dotted lines (St = 2.33, $L^+ = 24$, Re$_\tau$ = 180), finite-size simulations [63].

[14] and preferential alignment was less strong. In addition, the present Reynolds number based on the friction velocity, Re$_\tau$ (=435), was much higher than in the experiments by Hoseini *et al.* [14] (Re$_\tau$ = 170), presumably leading to a more "random" fiber orientation in the present measurements.

Up to this point, we have discussed the in-plane fiber orientations. However, in contrast to previous experiments [14,43], the present measurements resolve the 3D fiber orientation that can be represented by the fiber's direction cosines, $\cos \theta_x$, $\cos \theta_y$, and $\cos \theta_z$. The latter provide a measure for the alignment of the fiber's unit orientation vector, $\boldsymbol{p}$, onto the coordinate axes, x, y, and z, respectively [27]. Ensemble averaged values of the magnitudes of the direction cosines are presented in Fig. 9 together with relevant results from numerical simulations reported by Marchioli *et al.* [29], Andersson *et al.* [67], and Do-Quang *et al.* [63]. Note that the numerical simulations were all performed at much lower Re$_\tau$ (=180 for [63,67] and Re$_\tau$ = 150 for [29]) than the present

investigation ($\mathrm{Re}_\tau = 435$). In addition, Stokes numbers were much higher ($\mathrm{St} \geqslant 2.33$) in the numerical simulations than in the present experiments. Furthermore, the three numerical studies employed different modeling approaches; i.e., Marchioli *et al.* [29] and Andersson *et al.* [67] used the point-particle approach (the latter including two-way coupling), while Do-Quang *et al.* [63] accounted for the finite size of the fibers. As observed in Fig. 9, despite general similarities in the trends of the direction cosines upon approaching the wall, significant differences between the different numerical approaches are seen.

Starting with a closer look at fiber alignment with the streamwise direction, we note that the wall-normal distribution of $\overline{|\cos\theta_x|}$ [Fig. 9(a)] is similar to that of $\overline{|\cos\phi_{xy}|}$ (Fig. 6). Alignment with the streamwise direction is strongest near the wall at around $y^+ \approx 30$ in agreement with the results by Andersson *et al.* [67] (black solid lines in Fig. 9). Andersson *et al.* [67] showed that compared to Marchioli *et al.* [29] (one-way coupling, blue lines in Fig. 9) the peak in $\overline{|\cos\theta_x|}$ slightly shifted away from the wall when two-way coupling was accounted for. In contrast, the simulations by Do-Quang *et al.* [63] do not indicate a local wall-normal peak and values of $\overline{|\cos\theta_x|}$ continuously decrease with increasing y^+. The present measurements indicate that values of $\overline{|\cos\theta_x|}$ drop to "plateau" values of about 0.55 away from the wall ($y^+ > 100$). There are no striking differences in values of $\overline{|\cos\theta_x|}$ for the two investigated fiber types.

Fiber alignment with the wall-normal direction is illustrated by $\overline{|\cos\theta_y|}$ as a function of y^+, shown in Fig. 9(b). For $y^+ > 100$, $\overline{|\cos\theta_y|}$ reaches plateau values close to $\overline{|\cos\theta_y|} \approx 0.5$, indicating random orientation. Upon approaching the wall, $\overline{|\cos\theta_y|}$ strongly decreases, and both fiber types lose any alignment with the wall-normal direction. Length effects become significant only close to the wall ($y^+ < 40$) where loss of alignment of t2 fibers ($L_2^+ = 50.8$) is stronger than that of t1 fibers ($L_1^+ = 27.8$). Note that the numerical simulations by Marchioli *et al.* [29] (point-particle approach, one-way coupling) predicted the correct plateau values irrespective of fiber length. The same approach including two-way coupling [67] predicted slightly higher plateau values while the finite-size simulations by Do-Quang *et al.* [63] indicate much lower plateau values, likely the result of four-way coupling. Further note that the strong loss in alignment close to the wall is obtained in all numerical simulations.

Fiber alignment with the transverse direction, $\overline{|\cos\theta_z|}$ [Fig. 9(c)], indicates that closest to the wall the longest t2 fibers preferentially align in the transverse direction and values of $\overline{|\cos\theta_z|}$ reach about 0.68. In contrast, the shorter t1 fibers do not preferentially align and values closest to the wall do not exceed $\overline{|\cos\theta_z|} \approx 0.5$, i.e., random orientation. In the wake region ($y^+ > 150$), $\overline{|\cos\theta_z|}$ reaches plateau values slightly below 0.5. With the exception of the numerical simulations by Do-Quang *et al.* [63], our results qualitatively correspond to the numerical results employing the point-particle approach [27,29,67]. Like in the present results, these numerical simulations indicate that upon approaching the wall $\overline{|\cos\theta_z|}$ values initially decrease, reaching a local minimum (for $y^+ < 50$), after which they strongly increase. However, quantitatively there are significant differences between the numerical results and the present experiments, likely owing to lower Reynolds numbers and modeling approaches employed in the numerical studies.

Overall, the numerical results that come closest to the present experimental results are those by Marchioli *et al.* [29] ($\mathrm{St} = 5$, $\beta = 3$, $\mathrm{Re}_\tau = 150$). However, the length effects that we observed in the experiments are not replicated in their simulations. Based on our results, it can be concluded that increasing the fiber length leads to more significant loss of alignment with the wall-normal direction and increased alignment with the transverse direction, z. Note that observed length effects on $\overline{|\cos\theta_x|}$ were weak in the present experiments. However, it is interesting to note that while peak alignment with the streamwise direction is slightly away from the wall ($y^+ \approx 30$) alignment with the transverse direction is strongest closest to the wall ($14 \leqslant y^+ < 24$).

C. Fiber rotation rates

In this section, the fiber rotation rates will be presented. Similarly as in the previous section, the normalized in-plane fiber rotation rates, $\dot{\phi}_{xy}^+$ and $\dot{\phi}_{xz}^+$, will be first presented, after which the fiber's
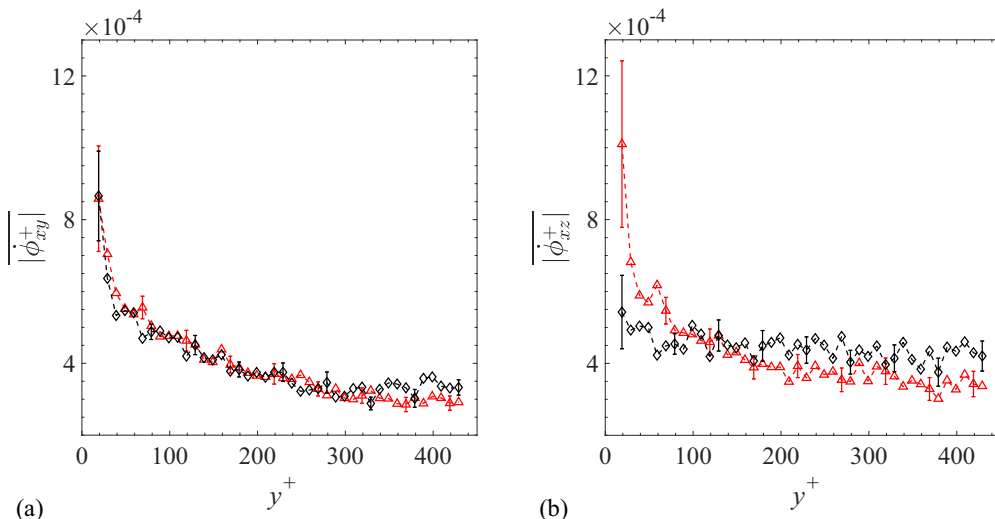
FIG. 10. Ensemble averaged magnitudes of the in-plane fiber angular velocities as a function of wall-normal position (bin size $\Delta y^+ = 10$). (a) $\overline{|\dot{\phi}_{xy}^+|}$. (b) $\overline{|\dot{\phi}_{xz}^+|}$. Fiber types: $\triangle$ t1, $\diamond$ t2. Representative error bars denote standard errors at 95% confidence intervals.

tumbling rates will be discussed. Note that the rotation rates are normalized by the viscous time scale, $\tau_v = \nu/u_\tau^2$, and indicate the angle in radians over which the fiber rotates within one viscous time scale.

The ensemble averaged magnitudes of the in-plane fiber rotation rates, $\overline{|\dot{\phi}_{xy}^+|}$ and $\overline{|\dot{\phi}_{xz}^+|}$, as a function of wall-normal distance are depicted in Fig. 10. As observed, the length difference between the t1 and t2 fibers does not affect $\overline{|\dot{\phi}_{xy}^+|}$ and the wall-normal distributions of $\overline{|\dot{\phi}_{xy}^+|}$ collapse for both fiber types [Fig. 10(a)]. In contrast, wall-normal distributions of $\overline{|\dot{\phi}_{xz}^+|}$ differ for t1 and t2 fibers [Fig. 10(b)]. In the wake region ($y^+ > 150$), $\overline{|\dot{\phi}_{xz}^+|}_{t2} > \overline{|\dot{\phi}_{xz}^+|}_{t1}$, while, closer to the wall ($y^+ < 100$), $\overline{|\dot{\phi}_{xz}^+|}_{t1} > \overline{|\dot{\phi}_{xz}^+|}_{t2}$. Further note that while $\overline{|\dot{\phi}_{xz}^+|}_{t2}$ hardly increases close to the wall, $\overline{|\dot{\phi}_{xz}^+|}_{t1}$ strongly increases and becomes almost twice as high as $\overline{|\dot{\phi}_{xz}^+|}_{t2}$ closest to the wall. These results are puzzling and hint at an intricate coupling between fiber lengths and the anisotropy in the wall-bounded flow structures in the transverse and wall-normal directions [68]. The near-wall region in a turbulent boundary layer is populated by coherent structures that may extend up to $3000x^+$ units in the streamwise direction and exhibit transverse coherency of about $100z^+$ units [12]. It is well known from measurements of fiber rotation in isotropic turbulence (no mean shear) that fiber rotation is dictated by "eddy" sizes of the order of the fiber length [23,66,69]. It is likely that away from the wall the longest t2 fibers are affected by larger, more energetic structures and therefore rotate faster in the x-z plane. On the other hand, rotation in the x-y plane is mostly affected by the strong mean (shear) flow in this plane and less affected by the turbulence structures advected by it.

Additional insight into the in-plane fiber rotation rates can be obtained from the PDF's of $\dot{\phi}_{xy}^+$ and $\dot{\phi}_{xz}^+$ in different wall-normal regions presented in Fig. 11. As expected [see Fig. 10(a)], the PDF's of $\dot{\phi}_{xy}^+$ (left column in Fig. 11) collapse for both fiber types in all regions of the turbulent boundary layer. Closest to the wall in the buffer layer [Fig. 11(a)], PDF's of $\dot{\phi}_{xy}^+$ are negatively skewed, indicating that the fibers preferentially rotate in the direction of the transverse component of the vorticity that is negative near the wall (not shown). Note that the latter is dictated by the wall-normal derivative of the streamwise velocity. Further away from the wall, the PDF's of $\dot{\phi}_{xy}^+$ become symmetric with increasing kurtosis values (not shown). The PDF's of $\dot{\phi}_{xz}^+$ (right column in Fig. 11) for both fiber
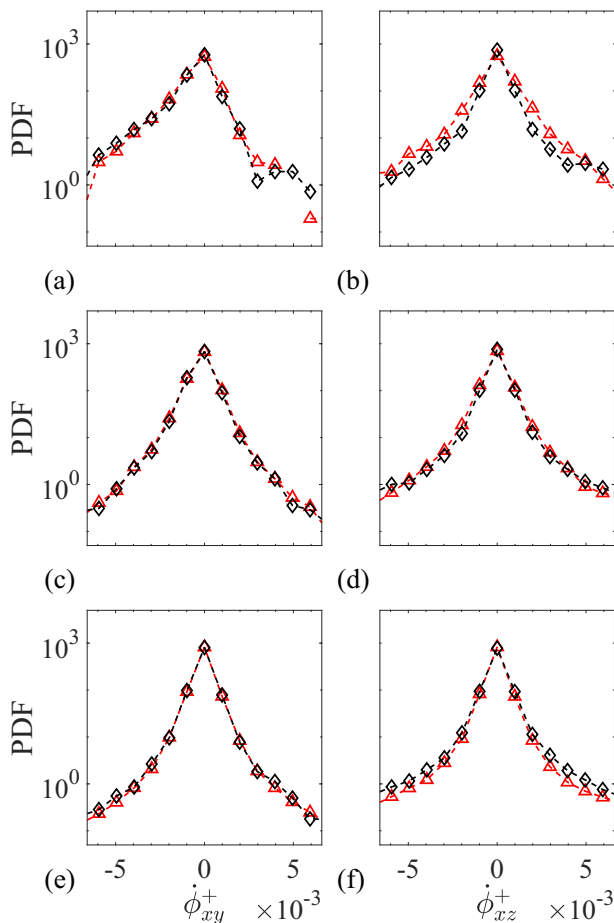
FIG. 11. PDF's of the normalized, fiber in-plane angular velocities in different regions of the turbulent boundary layer. Left column, $\dot{\phi}_{xy}^+$; right column, $\dot{\phi}_{xz}^+$. (a), (b) $14 < y^+ \leqslant 30$ (buffer layer). (c), (d) $30 < y^+ \leqslant 150$ (log layer). (e), (f) $150 < y^+ \leqslant 430$ (wake region).

types are symmetric in all cases, and differ in the buffer layer [Fig. 11(b)] as well as the wake region [Fig. 11(f)] in agreement with the distribution of $\overline{|\dot{\phi}_{xz}^+|}$ [see Fig. 10(b)]. In the wake region, t2 fibers indicate higher probabilities of extreme events of $\dot{\phi}_{xz}^+$ than t1 fibers. In the buffer layer, the opposite is observed. Note that in general PDF's of $\dot{\phi}_{xz}^+$ broaden upon approaching the wall, which can be associated with increased turbulence activity in the buffer layer. Similar "broadening" of fluctuating fiber rotation was observed in planar, wall-parallel measurements (at $y^+ = 14$, 43, and 72) by Hoseini *et al.* [14] for fibers with $\beta = 7$ and 14. For longer fibers, $\beta = 28$, they obtained the broadest PDF at $y^+ = 43$; however, differences between the various investigated wall-normal positions were small. They did not investigate fibers with $\beta > 28$.

The obtained distributions of $\overline{|\dot{\phi}_{xz}^+|}$ [Fig. 10(b)] and the PDF's of $\dot{\phi}_{xz}^+$ [Fig. 11(b)] in the buffer layer hint at intricate length effects in the buffer layer. The results clearly show that in the buffer layer extreme $\dot{\phi}_{xz}^+$ events of t2 fibers ($\overline{L}_{t2}^+ = 50.8$) are reduced compared to t1 fibers ($\overline{L}_{t1}^+ = 27.7$). We surmise that this result is related to the increased alignment of t2 fibers with the transverse direction [see Fig. 9(c)], leading to a more "stable" orientation of t2 fibers close to the wall. Furthermore, upon approaching the wall, turbulence structures become smaller, which makes it plausible that effects of small-scale turbulence structures "average" out with increasing fiber length. Most likely
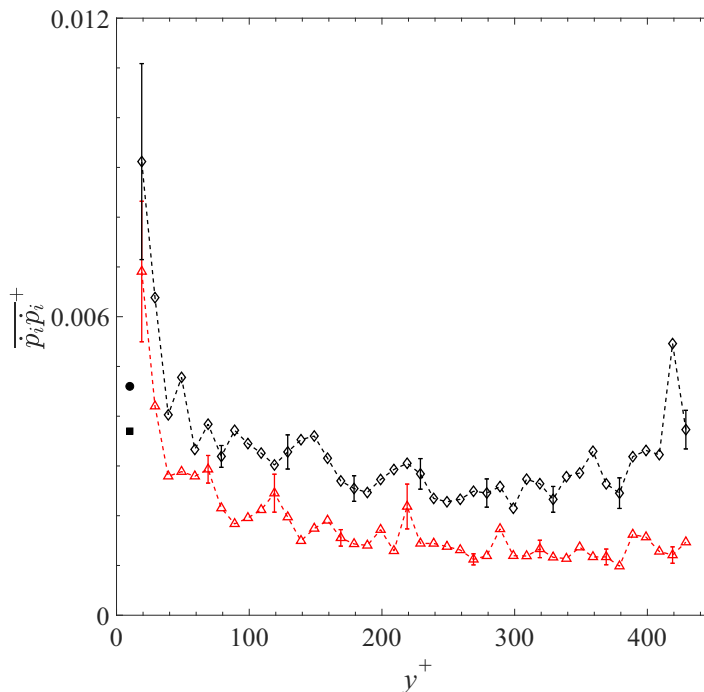
FIG. 12. Normalized, mean-squared tumbling rate of the fibers. Present data: fiber types △ t1, ◇ t2. Representative error bars denote standard errors at 95% confidence intervals. Numerical simulations: ● (St = 0, $\beta \simeq 16$), ■ (St = 1, $\beta \simeq 16$) at $y^+ = 10$ (Zhao *et al.* [32]).

these two effects act in tandem. Further note that in the log layer ($30 < y^+ \leqslant 150$, Fig. 10) length effects do not seem to play a role, which is in agreement with Marchioli and Soldati [21], but in contrast to the results by Hoseini *et al.* [14], who showed broadening of the PDF's at $y^+ = 72$ with increasing β. We also investigated if there was any correlation between V_x^+ and the in-plane fiber rotation rates. However, our results did not show such a correlation (not shown).

Our measurement setup also enabled the calculation of the fiber's tumbling rate based on the measured polar angle θ, its rotation rate $\dot{\theta}$, and the in-plane rotation rate $\dot{\phi}_{xy}$ [see Eq. (3)]. The mean-squared fiber tumbling rate, $\overline{\dot{p}_i \dot{p}_i}$, normalized by inner wall parameters is depicted in Fig. 12. Note that in order to remove spurious data points only data points within three standard deviations were considered in each bin. The results clearly show that the tumbling rate of the longest t2 fibers ($\overline{L}_{t2}^+ = 50.8$) exceeds that of the t1 fibers ($\overline{L}_{t1}^+ = 27.7$) across the whole measurement range. Although somewhat scattered, values of $(\overline{\dot{p}_i \dot{p}_i})_{t2}^+$ are almost twice those of the t1 fibers. It is well known that in isotropic turbulence fiber rotation is governed by turbulent eddies having spatial scales comparable to fiber lengths [23,66,70]. Therefore, we believe that the longest t2 fibers tumble faster than the shorter t1 fibers, since the former's rotation rates are dictated by larger scale, more energetic eddies.

Comparing our data to two available numerical data points ($y^+ = 10$) employing the point-particle approach [32] (Re_τ, $\beta = 16$) indicates that our values are of the same order of magnitude as the numerical ones. However, Zhao *et al.* [32] did not report the change of $\overline{\dot{p}_i \dot{p}_i}^+$ with wall-normal position, and it is unclear if they observed an increase in $\overline{\dot{p}_i \dot{p}_i}^+$ close to the wall as in the present measurements.

The PDF's of $(\dot{p}_i \dot{p}_i)^+$ in different regions of the boundary layer are presented in Fig. 13 for the two fiber types. As observed, PDF's of $(\dot{p}_i \dot{p}_i)_{t2}^+$ (left column in Fig. 13) exhibit tails of extreme tumbling rates at higher probabilities than those of $(\dot{p}_i \dot{p}_i)_{t1}^+$. Closest to the wall in the buffer layer
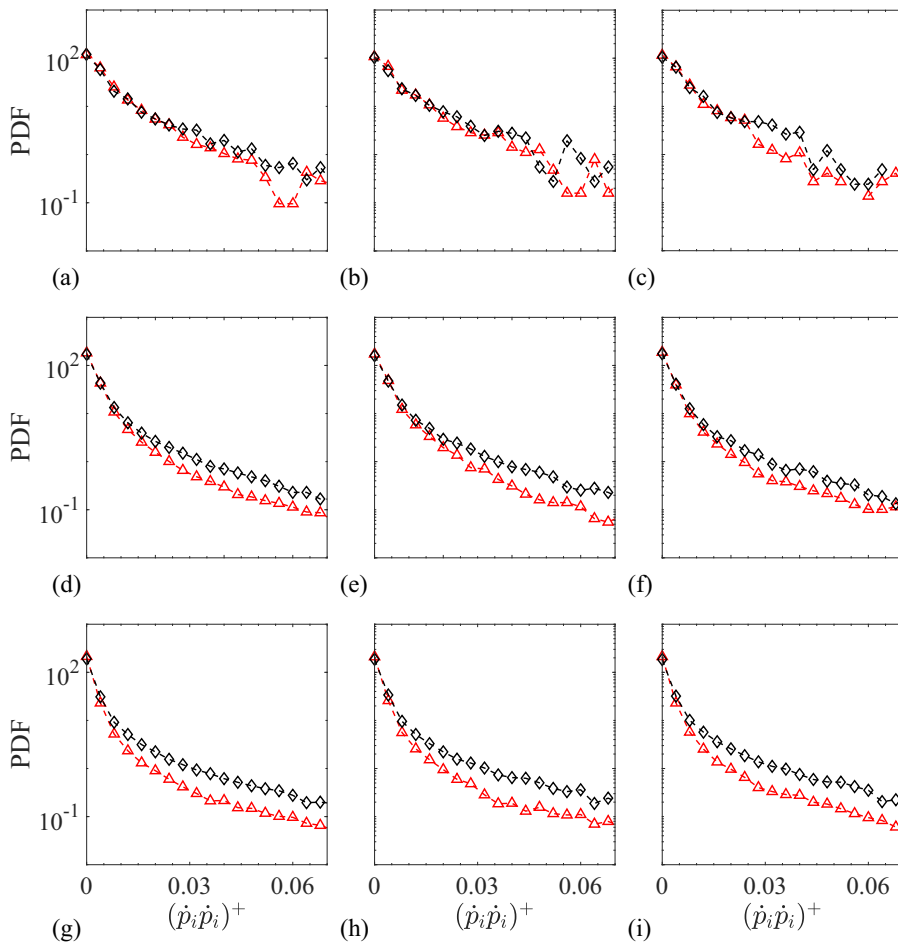
FIG. 13. PDF's of instantaneous, normalized fiber tumbling rates in different regions of the turbulent boundary layer. Top row, $14 < y^+ < 30$ (buffer layer); middle row, $30 < y^+ < 150$ (log layer); bottom row, $150 < y^+ < 430$ (wake region). Fiber types: △ t1, ◇ t2. Conditionally sampled data sets: ascending (middle column) and descending fibers (right column).

[Fig. 13(a)], the difference is small but it becomes increasingly pronounced upon moving away from the wall [Figs. 13(d) and 13(g)]. We also conditionally sampled the data set on "strong ascending" and "strong descending" fibers, similar as described in Sec. III A (Fig. 3), and the corresponding PDF's of the tumbling rates are plotted in the middle and right column (Fig. 13), respectively. The results do not show any striking difference between strong ascending and strong descending fibers and their tumbling rates do not seem to be much affected by preferential sampling of high- and low-speed flow regions [see Fig. 3(b)]. In addition, there is no clear change in the general observation that t2 fibers are characterized by higher probabilities of extreme events of $(\dot{p}_i \dot{p}_i)^+$.

IV. SUMMARY AND CONCLUSIONS

In this paper we reported on detailed measurements of the translational velocities, orientations, and rotational dynamics of rigid, nylon fibers in a turbulent, water channel flow ($\mathrm{Re}_\tau = 435$). The focus was on the investigation of length effects and to this purpose two different fiber types were investigated having similar Stokes numbers but significantly different lengths, $\overline{L}_{t1}^+ = 27.7$,

and $\overline{L}_{t2}^{+} = 50.8$. The measurements were performed using two-orthogonal view, digital holographic cinematography that enabled us to determine the 3D orientations of the fibers. Measured, ensemble averaged fiber velocities lagged the fluid velocity outside of the buffer layer as a result of fiber inertia. The longest t2 fibers lagged the most as a result of increased drag. However, closest to the wall ($14 \leqslant y^{+} < 24$), fiber velocities exceeded those of the fluid, in agreement with numerical simulations taking the finite particle size into account, but in disagreement with available simulations employing the point-particle approach. This excess velocity of the fibers close to the wall is the result of preferential accumulation of the fibers in high-speed streaks and the only other known experimental evidence for this was published in the Ph.D. dissertation by Hoseini [64].

We further investigated the PDF's of the instantaneous components of the fiber centroid velocities and found that the longer t2 fibers have higher probabilities of extreme high magnitude events of the wall-normal and transverse velocities, especially in the log layer and the wake region. Since length effects are mostly at play here, these increased probabilities are likely the result of the interaction of the longer t2 fibers with larger scale turbulent structures and associated increased hydrodynamic torques acting on them. In contrast, besides a slight shift in the mean, the shapes of the PDF's of V_x^{+} were similar for both fiber types. Furthermore, in the buffer layer, PDF's of V_x^{+} and V_y^{+} collapsed for the t1 and t2 fibers, despite their length difference and proximity to the wall. We believe that, although the longest investigated fiber ($\overline{L}_{t2}^{+} = 50.8$) was long enough to interact with the wall at the smallest wall-normal measurement position ($y^{+} = 14$), in practice, fibers did not make contact with the bottom wall as a result of preferential alignment with the streamwise direction upon approaching the wall. Our measurements showed that both t1 and t2 fibers preferentially align with the streamwise direction both in the wall-parallel as well as in the wall-normal plane, and lose any alignment with the wall-normal direction. Therefore, close to the wall the fibers are preferentially oriented with their major axes parallel to the wall, limiting fiber-wall interaction.

Regarding fiber rotation, our results indicated that the wall-normal distributions of the mean magnitudes of the fiber in-plane rotation rates were similar in the x-y plane for both fiber types but dissimilar in the x-z plane. In the x-y plane, fiber rotation rates increased strongly upon approaching the wall while in the x-z plane this was only observed for the shorter t1 fibers. Values of $|\dot{\phi}_{xz}^{+}|$ of the longer t2 fibers remained almost constant with wall-normal position. These results indicate that for the present investigated fiber types length effects are mainly "felt" in the x-z plane where mean flow gradients are small.

Wall-normal distributions of the mean-squared fiber tumbling rates indicated a strong increase of the tumbling rate in the buffer layer for both investigated fiber types. In contrast, in the log layer and the wake region, values of $\overline{\dot{p}_i \dot{p}_i}^{+}$ remain nearly constant. We observed a clear effect of the length difference between the two fiber types. The longest t2 fibers tumbled consistently at a higher rate than the shorter t1 fibers. We attribute this to the interaction of the longer fibers with larger, more energetic turbulence structures.

As far as we are aware, these are the first detailed measurements of 3D fiber orientations and rotation rates in a turbulent boundary layer flow. In the future, we plan to investigate a wider range of Stokes numbers and fiber lengths.

ACKNOWLEDGMENTS

---

[1] G. A. Voth and A. Soldati, Anisotropic particles in turbulence, Annu. Rev. Fluid Mech. **49**, 249 (2017).

[2] F. Lundell, L. D. Söderberg, and P. H. Alfredsson, Fluid mechanics of papermaking, Annu. Rev. Fluid Mech. **43**, 195 (2011).

[3] T. D. Papathanasiou and D. C. Guell, *Flow-Induced Alignment in Composite Materials* (Woodhead publishing, 1997), p. 384.

[4] M. J. Shultz, Crystal growth in ice and snow, Phys. Today **71**, 34 (2018).

[5] J. E. Kristjánsson, J. M. Edwards, and D. L. Mitchell, Impact of a new scheme for optical properties of ice crystals on climates of two GCMs, J. Geophys. Res. **105**, 10063 (2000).

[6] S. B. Pope, *Turbulent Flows* (Cambridge University, Cambridge, England, 2000).

[7] S. K. Robinson, Coherent motions in the turbulent boundary layer, Annu. Rev. Fluid Mech. **23**, 601 (1991).

[8] J. Zhou, R. J Adrian, S. Balachandar, and T. M. Kendall, Mechanisms for generating coherent packets of hairpin vortices in channel flow, J. Fluid Mech. **387**, 353 (1999).

[9] W. W. Willmarth and S. S. Lu, Structure of the Reynolds stress near the wall, J. Fluid Mech. **55**, 65 (1972).

[10] R. van Hout, Spatially and temporally resolved measurements of bead resuspension and saltation in a turbulent water channel flow, J. Fluid Mech. **715**, 389 (2013).

[11] A. Soldati, Particles turbulence interactions in boundary layers, Z. Angew. Math. Mech. **85**, 683 (2005).

[12] R. J. Adrian, Hairpin vortex organization in wall turbulence, Phys. Fluids **19**, 041301 (2007).

[13] N. R. Challabotla, L. Zhao, and H. I. Andersson, Shape effects on dynamics of inertia-free spheroids in wall turbulence, Phys. Fluids **27**, 061703 (2015).

[14] A. A. Hoseini, F. Lundell, and H. I. Andersson, Finite-length effects on dynamical behavior of rod-like particles in wall-bounded turbulent flow, Int. J. Multiphase Flow **76**, 13 (2015).

[15] G. B. Jeffery, The motion of ellipsoidal particles immersed in a viscous fluid, Proc. R. Soc. A **102**, 161 (1922).

[16] R. K. Newsom and C. W. Bruce, Orientational properties of fibrous aerosols in atmospheric turbulence, J. Aerosol Sci. **29**, 773 (1998).

[17] O. Bernstein and M. Shapiro, Direct determination of the orientation distribution function of cylindrical particles immersed in laminar and turbulent shear flows, J. Aerosol Sci. **25**, 113 (1994).

[18] J. A. Olson and R. J. Kerekes, The motion of fibres in turbulent flow, J. Fluid Mech. **377**, 47 (1998).

[19] J. A. Olson, The motion of fibres in turbulent flow, stochastic simulation of isotropic homogeneous turbulence, Int. J. Multiphase Flow **27**, 2083 (2001).

[20] M. Parsheh, M. L. Brown, and C. K. Aidun, On the orientation of stiff fibres suspended in turbulent flow in a planar contraction, J. Fluid Mech. **545**, 245 (2005).

[21] C. Marchioli and A. Soldati, Rotation statistics of fibers in wall shear turbulence, Acta Mech. **224**, 2311 (2013).

[22] L. Sabban, A. Cohen, and R. van Hout, Temporally resolved measurements of heavy, rigid fibre translation and rotation in nearly homogeneous isotropic turbulence, J. Fluid Mech. **814**, 42 (2017).

[23] S. Kuperman, L. Sabban, and R. van Hout, Inertial effects on the dynamics of rigid heavy fibers in isotropic turbulence, Phys. Rev. Fluids **4**, 064301 (2019).

[24] S. Parsa, J. S. Guasto, M. Kishore, N. T. Ouellette, J. P. Gollub, and G. A. Voth, Rotation and alignment of rods in two-dimensional chaotic flow, Phys. Fluids **23**, 043302 (2011).

[25] L. Zhao and H. I. Andersson, Why spheroids orient preferentially in near-wall turbulence, J. Fluid Mech. **807**, 221 (2016).

[26] Y. Jie, C. Xu, J. R. Dawson, H. I. Andersson, and L. Zhao, Influence of the quiescent core on tracer spheroidal particle dynamics in turbulent channel flow, Journal of Turbulence **20**, 424 (2019).

[27] P. H. Mortensen, H. I. Andersson, J. J. J. Gillissen, and B. J. Boersma, Dynamics of prolate ellipsoidal particles in a turbulent channel flow, Phys. Fluids **20**, 093302 (2008).

[28] Z. Cui, A. Dubey, L. Zhao, and B. Mehlig, Alignment statistics of rods with the Lagrangian stretching direction in a channel flow, J. Fluid Mech. **901**, A16 (2020).

[29] C. Marchioli, M. Fantoni, and A. Soldati, Orientation, distribution, and deposition of elongated, inertial fibers in turbulent channel flow, Phys. Fluids **22**, 033301 (2010).

[30] C. Marchioli, L. Zhao, and H. I. Andersson, On the relative rotational motion between rigid fibers and fluid in turbulent channel flow, Phys. Fluids **28**, 013301 (2016).

[31] L. H. Zhao, H. I. Andersson, and J. J. J. Gillissen, On inertial effects of long fibers in wall turbulence: Fiber orientation and fiber stresses, Acta Mech. **224**, 2375 (2013).

[32] L. Zhao, N. R. Challabotla, H. I. Andersson, and E. A. Variano, Rotation of Nonspherical Particles in Turbulent Channel Flow, Phys. Rev. Lett. **115**, 244501 (2015).

[33] J. J. J. Gillissen, B. J. Boersma, P. H. Mortensen, and H. I. Andersson, On the performance of the moment approximation for the numerical computation of fiber stress in turbulent channel flow, Phys. Fluids **19**, 035102 (2007).

[34] F. Zhao, W. K. George, and B. G. M. Van Wachem, Four-way coupled simulations of small particles in turbulent channel flow: The effects of particle shape and stokes number, Phys. Fluids **27**, 083301 (2015).

[35] J. K. Eaton, Two-way coupled turbulence simulations of gas-particle flows using point-particle tracking, Int. J. Multiphase Flow **35**, 792 (2009).

[36] S. Balachandar, A scaling analysis for point–particle approaches to turbulent multiphase flows, Int. J. Multiphase Flow **35**, 801 (2009).

[37] H. Zhang, G. Ahmadi, F.-G. Fan, and J. B. McLaughlin, Ellipsoidal particles transport and deposition in turbulent channel flows, Int. J. Multiphase Flow **27**, 971 (2001).

[38] L. Zhao, N. R. Challabotla, H. I. Andersson, and E. A. Variano, Mapping spheroid rotation modes in turbulent channel flow: Effects of shear, turbulence and particle inertia, J. Fluid Mech. **876**, 19 (2019).

[39] K. Yang, L. Zhao, and H. I. Andersson, Mean shear versus orientation isotropy: Effects on inertialess spheroids' rotation mode in wall turbulence, J. Fluid Mech. **844**, 796 (2018).

[40] R. Holm and D. Söderberg, Shear influence on fibre orientation, Rheol. Acta **46**, 721 (2007).

[41] E. Gavze and M. Shapiro, Particles in a shear flow near a solid wall: Effect of nonsphericity on forces and velocities, Int. J. Multiphase Flow **23**, 155 (1997).

[42] L. Jianzhong, Z. Weifeng, and Yu. Zhaosheng, Numerical research on the orientation distribution of fibers immersed in laminar and turbulent pipe flows, J. Aerosol Sci. **35**, 63 (2004).

[43] A. Capone and G. P. Romano, Interactions between fluid and fibers in a turbulent backward-facing step flow, Phys. Fluids **27**, 053303 (2015).

[44] R. van Hout, A. Krakovich, and O. Gottlieb, Time resolved measurements of vortex-induced vibrations of a tethered sphere in uniform flow, Phys. Fluids **22**, 087101 (2010).

[45] R. van Hout, Time-resolved PIV measurements of the interaction of polystyrene beads with near-wall-coherent structures in a turbulent channel flow, Int. J. Multiphase Flow **37**, 346 (2011).

[46] G. E. Elsinga and J. Westerweel, Tomographic-PIV measurement of the flow around a zigzag boundary layer trip, Exp. Fluids **52**, 865 (2012).

[47] C. S. Vikram, *Particle Field Holography* (Cambridge University, Cambridge, England, 2005), Vol. 11.

[48] B. Rabencov, J. Arca, and R. van Hout, Measurement of polystyrene beads suspended in a turbulent square channel flow: Spatial distributions of velocity and number density, Int. J. Multiphase Flow **62**, 110 (2014).

[49] M. Shapiro and M. Goldenberg, Deposition of glass fiber particles from turbulent air flow in a pipe, J. Aerosol Sci. **24**, 65 (1993).

[50] L. Zhao and H. I. Andersson, On particle spin in two-way coupled turbulent channel flow simulations, Phys. Fluids **23**, 093302 (2011).

[51] B. Herzhaft and É. Guazzelli, Experimental study of the sedimentation of dilute and semi-dilute suspensions of fibres, J. Fluid Mech. **384**, 133 (1999).

[52] J. Happel and H. Brenner, *Low Reynolds Number Hydrodynamics: With Special Applications to Particulate Media* (Springer, New York, 2012), Vol. 1.

[53] R. Clift, J. R. Grace, and M. E. Weber, *Bubbles, Drops, and Particles* (Courier, New York, 2005).

[54] S. Elghobashi, On predicting particle-laden turbulent flows, Appl. Sci. Res. **52**, 309 (1994).

[55] J. H. Milgram and W. Li, Computational reconstruction of images from holograms, Appl. Opt. **41**, 853 (2002).

[56] R. van Hout, L. Sabban, and A. Cohen, The use of high-speed PIV and holographic cinematography in the study of fiber suspension flows, Acta Mech. **224**, 2263 (2013).

[57] U. Schnars and W. Jüptner, *Digital Holography: Digital Hologram Recording, Numerical Reconstruction, and Related Techniques* (Springer-Verlag, Berlin, 2005).

[58] J. Sheng, E. Malkiel, and J. Katz, Digital holographic microscope for measuring three-dimensional particle distributions and motions, Appl. Opt. **45**, 3893 (2006).

[59] M. Righetti and G. P. Romano, Particle-fluid interactions in a plane near-wall turbulent flow, J. Fluid Mech. **505**, 93 (2004).

[60] F. Picano, W.-P. Breugem, and L. Brandt, Turbulent channel flow of dense suspensions of neutrally buoyant spheres, J. Fluid Mech. **764**, 463 (2015).

[61] L.-P. Wang, C. Peng, Z. Guo, and Z. Yu, Flow modulation by finite-size neutrally buoyant particles in a turbulent channel flow, J. Fluids Eng. **138**, 041306 (2016).

[62] C. Zhu, Z. Yu, and X. Shao, Interface-resolved direct numerical simulations of the interactions between neutrally buoyant spheroidal particles and turbulent channel flows, Phys. Fluids **30**, 115103 (2018).

[63] M. Do-Quang, G. Amberg, G. Brethouwer, and A. V. Johansson, Simulation of finite-size fibers in turbulent channel flows, Phys. Rev. E **89**, 013006 (2014).

[64] A. A. Hoseini, Experimental study of turbulent flow with dispersed rod-like particles through optical measurements, Doctoral thesis, Norwegian University of Science and Technology NTNU - Trondheim, 2014.

[65] L. Zhao, C. Marchioli, and H. I. Andersson, Slip velocity of rigid fibers in turbulent channel flow, Phys. Fluids **26**, 063302 (2014).

[66] S. Bounoua, G. Bouchet, and G. Verhille, Tumbling of Inertial Fibers in Turbulence, Phys. Rev. Lett. **121**, 124502 (2018).

[67] H. I. Andersson, L. Zhao, and M. Barri, Torque-coupling and particle-turbulence interactions, J. Fluid Mech. **696**, 319 (2012).

[68] H. I. Andersson, L. Zhao, and E. A. Variano, On the anisotropic vorticity in turbulent channel flows, J. Fluids Eng. **137**, 084503 (2015).

[69] A. D. Bordoloi and E. Variano, Rotational kinematics of large cylindrical particles in turbulence, J. Fluid Mech. **815**, 199 (2017).

[70] S. Parsa and G. A. Voth, Inertial Range Scaling in Rotations of Long Rods in Turbulence, Phys. Rev. Lett. **112**, 024501 (2014).